Nanoscale Advances

ROYAL SOCIETY OF CHEMISTRY

PAPER

Cite this: *Nanoscale Adv.*, 2023, **5**, 2061

Facile synthesis of crumpled nitrogen-doped porous carbon nanosheets with ultrahigh surface area for high-performance supercapacitors†

Chong Chen, *[a] Jiacan Shao,[b] Yaru Zhang,[a] Li Sun,[a] Keying Zhang,[a] Hongyan Wang,[a] Guang Zhu*[ab] and Xusheng Xie[a]

Porous carbon nanosheets are currently considered excellent electrode materials for high-performance supercapacitors. However, their ease of agglomeration and stacking nature reduce the available surface area and limit the electrolyte ion diffusion and transport, thereby leading to low capacitance and poor rate capability. To solve these problems, we report an adenosine blowing and KOH activation combination strategy to prepare crumpled nitrogen-doped porous carbon nanosheets (CNPCNS), which exhibit much higher specific capacitance and rate capability compared to flat microporous carbon nanosheets. The method is simple and capable of one-step scalable production of CNPCNS with ultrathin crumpled nanosheets, ultrahigh specific surface area (SSA), microporous and mesoporous structure and high heteroatom content. The optimized CNPCNS-800 with a thickness of 1.59 nm has an ultrahigh SSA of 2756 m^2 g^{-1}, high mesoporosity of 62.9% and high heteroatom content (2.6 at% for N, 5.4 at% for O). Consequently, CNPCNS-800 presents an excellent capacitance, high rate capability and long cycling stability both in 6 M KOH and $EMIMBF_4$. More importantly, the energy density of the CNPCNS-800-based supercapacitor in $EMIMBF_4$ can reach up to 94.9 W h kg^{-1} at 875 W kg^{-1} and is still 61.2 W h kg^{-1} at 35 kW kg^{-1}.

Received 26th December 2022
Accepted 20th February 2023

DOI: 10.1039/d2na00949h

rsc.li/nanoscale-advances

Introduction

The development of energy storage devices has played a vital role in the development of renewable energy sources.[1–3] Nowadays, carbon-based supercapacitors are considered as one of the most promising next-generation energy storage devices, primarily due to their high power density, rapid charge–discharge rate and long cycle life.[4] Although lacking adequate fast electrolyte ion diffusion channels for inner-pore ion transport at high-rate, activated carbon is still utilized as the electrode material in commercial supercapacitors. However, the low energy density and poor rate performance of commercial activated carbon-based supercapacitors impede their widespread application. Therefore, extensive effort has been devoted to designing and preparing various advanced nanostructured carbonaceous electrode materials for improving the capacitance and rate performance without sacrificing the long cycle life, such as carbon nanosheets,[5,6] carbon nanocages,[7,8] carbon nanospheres,[9,10] and graphene.[11–14]

Among various carbon electrode nanomaterials, carbon nanosheets have attracted extensive attention in supercapacitors because of their microscale lateral size with nanoscale thickness, high specific surface area (SSA) and unusual physicochemical properties.[15,16] According to the electric double-layer capacity (EDLC) storage mechanism, capacitance arises from charge accumulation at the electrode–electrolyte interfaces. Thus, carbon nanosheets with high SSA are greatly preferred. The two-dimensional planar structure and nanoscale thickness of carbon nanosheets make the inner-pores more easily exposed to the electrolyte during the charge and discharge process, which provides many active sites for ion physisorption and decreases the electrolyte ion diffusion distance, leading to low ionic transport resistance. However, the ease of agglomeration and stacking features of the flat and smooth nanosheets limit their accessible SSA, resulting in low capacitance. Moreover, the electrolyte ion diffusion path length is increased, leading to poor rate capability.[17–19] Tremendous strategies have been proposed to prevent the stacking effects of carbon nanosheets, such as the design of carbon nanosheet morphologies, optimization of carbon nanosheet pore structures, regulation of carbon nanosheet compositions, among others.[19–25] In our recent studies, we introduce the intercalation of space between the carbon nanosheets to prevent the carbon nanosheets from stacking for high-performance supercapacitors.[26,27] In addition, the development

[a]*Key Laboratory of Spin Electron and Nanomaterials of Anhui Higher Education Institutes, School of Chemistry and Chemical Engineering, Suzhou University, Suzhou 234000, People's Republic of China. E-mail: szxychenchong@163.com; guangzhu@ahszu.edu.cn*

[b]*School of Mechanics and Photoelectric Physics, Anhui University of Science and Technology, Huainan 232001, P. R. China*

† Electronic supplementary information (ESI) available. See DOI: https://doi.org/10.1039/d2na00949h

of crumpled carbon nanosheets has been considered as an effective and attractive approach to address this problem as the unique and highly crumpled structure could effectively prevent the stacking and aggregation of carbon nanosheets through intercalation of space in the carbon nanosheets and provide adequate fast electrolyte ion diffusion channels without sacrificing their high aspect ratio feature.[28,29] For example, the specific capacitance of highly crumpled carbon nanosheets is 294 F g^{-1} at 0.5 A g^{-1}.[30] The *Salvia splendens*-derived crumpled carbon nanosheets exhibit an ultrahigh capacitance retention of 88.6% at 100 A g^{-1}.[31] The rate performance of crumpled carbon nanosheets has been greatly improved but still suffers from low capacitance even at relatively low current density because of their insufficient SSA. Another efficient approach for improving the capacitance is doping nitrogen into carbon nanosheets as these nitrogen functionalities could generate additional pseudocapacitance. Therefore, it is highly desirable to obtain the crumpled carbon nanosheets with large SSA and high nitrogen doping content.

Inspired by our previous work on the calcium D-gluconate-exploding method for making carbon nanosheets,[27] herein we developed an adenosine blowing and KOH activation combination method to synthesize crumpled nitrogen-doped porous carbon nanosheets (CNPCNS). It is capable of one-step scalable production of CNPCNS with large SSA and high nitrogen doping content. Adenosine consists of adenine and pentose, and acts as both carbon/nitrogen source and expansive agent to form nitrogen-doped carbon nanosheets. Moreover, with its large number of pores, the formed crumpled nanosheets structure is simultaneously dependent on high corrosion through the KOH activator in the carbonization process. CNPCNS has an ultrahigh SSA of 2756 m^2 g^{-1}, high mesoporosity of 62.9%, high heteroatom content (2.6 at% for N, 5.4 at% for O) and two-dimensional highly crumpled nanosheets structure with a thickness of 1.59 nm and a lateral dimension of dozens of micrometers. As a result, CNPCNS exhibits an outstanding specific capacitance, high rate capability and high cycling stability both in 6 M KOH and $EMIMBF_4$. More importantly, the energy density of the CNPCNS-based supercapacitor in $EMIMBF_4$ can reach up to 94.9 W h kg^{-1} at 875 W kg^{-1}, and is still as high as 61.2 W h kg^{-1} even at 35 kW kg^{-1}.

Experimental

Typically, 10 g adenosine (Aladdin, 99%) was ground with 10 g potassium hydroxide (KOH) (Macklin, 95%), and then the mixture was carbonized at 800 °C for 2 h under Ar atmosphere, with a heating rate of 5 °C min^{-1}. The obtained sample was washed with diluted HCl and distilled water, and then was dried at 100 °C for 12 h and classified as 'CNPCNS-800'. In addition, the control sample named NPCNS was prepared by the same procedure of CNPCNS-800 when the mass ratio of KOH and adenosine was 1 : 3. CNPCNS-700 and CNPCNS-900 were produced by the same procedure of CNPCNS-800, where 700, 800 and 900 were the pyrolysis temperatures.

The characterizations and electrochemical measurements are given in ESI.†

Results and discussion

In the process (Fig. 1), adenosine could act as both carbon/nitrogen source and expansive agent to prepare carbon nanosheets without adding any nitrogen source, which was different from previously reported sugar-blowing and calcium D-gluconate-exploding methods. Direct carbonization of adenosine or pentose without adding any KOH could achieve the formation of sheet-like structures (Fig. S1†), while direct carbonization of adenine could only obtain irregular micro-sized particles (Fig. S2†), indicating that pentose was the key component in adenosine and played an important role in forming sheet-like structures. The reason why the carbon nanosheet structure could be prepared by carbonizing adenosine was also attributed to pentose thermal polymerization and thermal expansion. KOH acted as an activator to regulate the morphology and pore structure of adenosine-derived nitrogen-doped carbon nanosheets.[32] When the mass ratio of KOH and adenosine was 1 : 3, the obtained sample named as NPCNS exhibited two dimensional (2D) micro-sized carbon nanosheets with a smooth and flat surface (Fig. 2a and b). The predominant micropores on the carbon nanosheets of NPCNS in the high-resolution TEM image (Fig. 2c) revealed the generation of abundant microporous structures after KOH activation. The smooth and flat surface of the carbon nanosheets could further be observed in TEM (Fig. S3†) and AFM images (Fig. 2d). The thickness of NPCNS was 4.69 nm.

When the mass ratio of KOH and adenosine was 1 : 1, CNPCNS-800 was formed (Fig. 2e and f) and exhibited 2D crumpled and curled carbon nanosheets with the thickness of 1.59 nm, which could be observed in the AFM image (Fig. 2g). The crumpled carbon nanosheets were much thinner than the flat carbon nanosheets. The relatively low thickness of the carbon nanosheets and the crumpled surface structure in CNPCNS-800 were due to the significantly stronger KOH activation, resulting in a large amount of carbon weight loss in the carbon nanosheets. When the activation temperatures were 700 °C and 900 °C, the crumpled carbon nanosheet architectures could be still maintained in CNPCNS-700 and CNPCNS-900, respectively (Fig. S4†). The crumpled and curled surface structure of CNPCNS-800 is clearly seen in the TEM image (Fig. 2h), which could prevent the carbon nanosheets from stacking together. The crumpled carbon nanosheets were randomly decorated with numerous mesopores at the flat and wrinkled region (Fig. 2i and j), which would provide more transportation and diffusion paths for electrolyte ion diffusion from the exterior to the interior of the carbon nanosheets. Fig. 2k displays the high-resolution TEM image of CNPCNS-800. Except for the mesopores, CNPCNS-800 had abundant micropores distributed throughout the whole crumpled carbon nanosheets, which were responsible for adsorbing and storing electrolyte ions. The EDX elemental mappings (Fig. S5†) of CNPCNS-800 revealed that nitrogen and oxygen atoms were successfully doped into the carbon framework even after strong corrosion by the KOH activator.

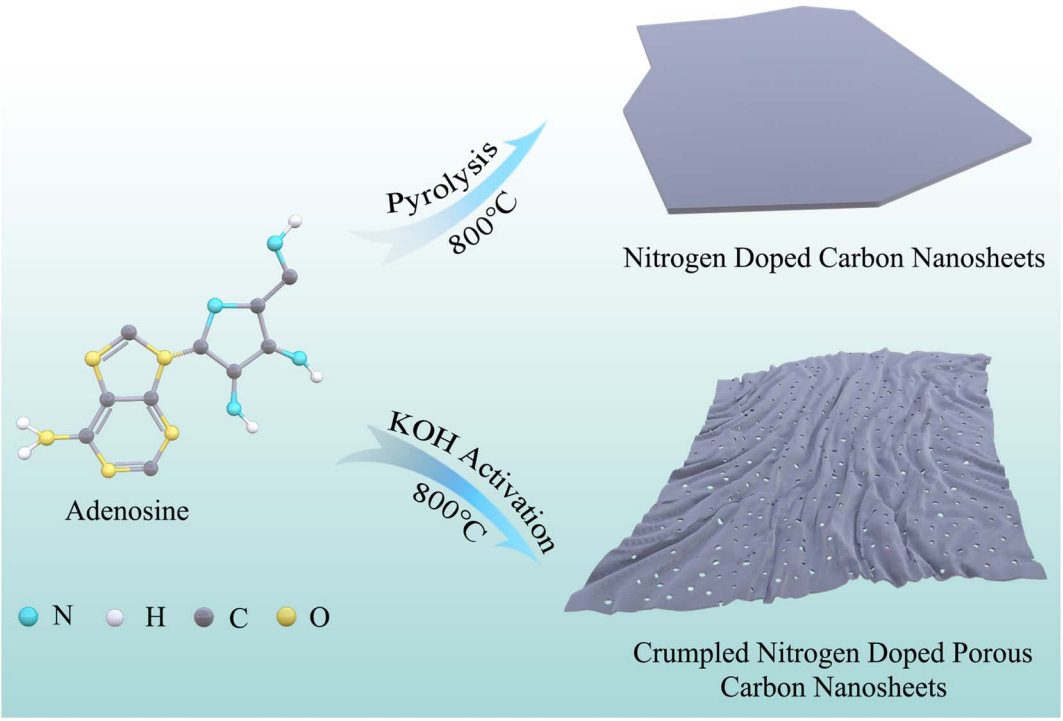

Fig. 1 Diagrammatic procedure for the preparation of the samples.

The crystallization nature of NPCNS, CNPCNS-700, CNPCNS-800 and CNPCNS-900 was studied by XRD and Raman spectroscopy. Fig. 3a exhibits the XRD patterns of NPCNS, CNPCNS-700, CNPCNS-800 and CNPCNS-900. Two broad and weak diffraction peaks were observed and located at 25° and 43°, which corresponded to the (002) and (100) reflections of graphite, respectively. Obviously, the peaks appearing at 25° of CNPCNS-800 and CNPCNS-900 had much weaker intensity compared with those of NPCNS and CNPCNS-700, indicating their much lower graphitization degree. The Raman spectra of NPCNS, CNPCNS-700, CNPCNS-800 and CNPCNS-900 are shown in Fig. 3b, in which two distinct peaks appeared at around 1351 cm^{-1} and 1594 cm^{-1} and correspond to the D-band and G-band, respectively. The D-band corresponded to the defect carbon structure and the G-band corresponded to the sp^2-hybridized graphitic carbon. The I_D/I_G (the intensity ratio of the D-band to G-band) was 1.02 for NPCNS, 1.05 for CNPCNS-700, 1.14 for CNPCNS-800 and 1.20 for CNPCNS-900, revealing the increasing amorphous degree after KOH activation.

The porous structures of NPCNS, CNPCNS-700, CNPCNS-800 and CNPCNS-900 were further evaluated by nitrogen physisorption measurements, and are shown in Fig. 3c. The isotherms of NPCNS presented I-type curve due to the predominant micropores in the sample. In sharp contrast, the isotherms of CNPCNS-700, CNPCNS-800 and CNPCNS-900 exhibited IV-type curves with a steep adsorption below 0.05 P/P_0 and a hysteresis loop starting at 0.4 P/P_0, indicating the coexistence of abundant micropores and mesopores in those samples, which was consistent with the TEM results. The pore properties of NPCNS, CNPCNS-700, CNPCNS-800 and CNPCNS-900 are listed in Table 1. The BET SSA of CNPCNS-800 reached up to 2756 $m^2\ g^{-1}$, which was higher than those of NPCNS, CNPCNS-700 and CNPCNS-900. The microporous surface area in CNPCNS-800 was much higher than those of NPCNS and CNPCNS-900, but was lower than that of CNPCNS-700, indicating that both micropores and mesopores were greatly developed in CNPCNS-800. It is noted that the microporosity in SSA progressively decreased from NPCNS to CNPCNS-900, while the mesoporosity in SSA continuously increased from NPCNS to CNPCNS-900, demonstrating a gradual deepening of the activation process after increasing both the amount of KOH and activation temperature. The microporous pore volume and microporosity in the total pore volume exhibited the same trend, as summarized in Table 1. As shown in Fig. S6,† the pore volumes were mainly contributed from pores within 1–3 nm for NPCNS and CNPCNS-700 and 1–6 nm for CNPCNS-800 and CNPCNS-900, which was further indicated from the pore size distributions of NPCNS, CNPCNS-700, CNPCNS-800 and CNPCNS-900 calculated according to DFT theory (Fig. 3d). NPCNS exhibited mostly micropores with the size mainly distributed at 0.6, 0.7, 0.8, and 1.2 nm. CNPCNS-700, CNPCNS-800 and CNPCNS-900 displayed a hierarchical porous structure with micropores similar to those of NPCNS and mesopores in the size range from 2 to 8 nm. The generation of micropores/mesopores in CNPCNS should be predominantly attributed to KOH thermal activation. The mesopores of CNPCNS-800 had a wider pore size distribution (2.0–6.0 nm) than that of CNPCNS-700 (2.0–4.0 nm), but were narrower than that of CNPCNS-900 (2.0–8.0 nm), indicating that the strong activation is favorable for mesopore generation. The 2D crumpled and

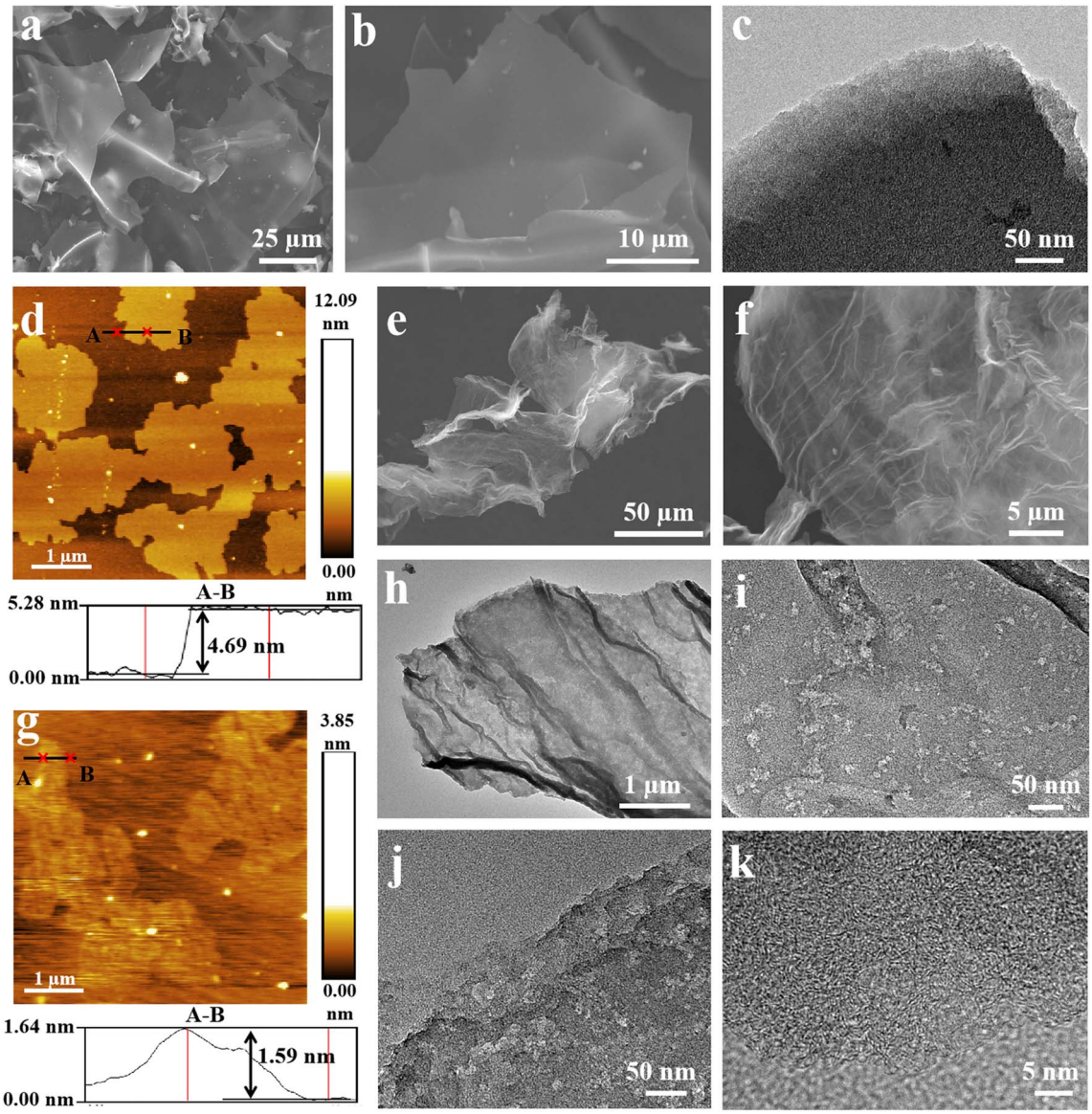

Fig. 2 (a and b) SEM, (c) TEM, and (d) AFM images of NPCNS. (e and f) SEM, (g) AFM, and (h–k) TEM images of CNPCNS-800.

curled nanosheet-like structure with the highest BET SSA and appropriate microporous/mesoporous structure of CNPCNS-800 demonstrate its potential as a promising electrode material for obtaining high performance in supercapacitors.

Elemental compositions of NPCNS, CNPCNS-700, CNPCNS-800 and CNPCNS-900 were investigated by XPS technique. The XPS survey spectra (Fig. 4a) of NPCNS, CNPCNS-700, CNPCNS-800 and CNPCNS-900 exhibited a predominant narrow C 1s peak at 285.1 eV and two narrow N 1s and O 1s weak peaks at 400.1 eV and 532.1 eV, respectively. The elemental contents of NPCNS, CNPCNS-700, CNPCNS-800 and CNPCNS-900 are listed in Table 1. Obviously, the contents of both N and O progressively decreased from NPCNS to CNPCNS-900, indicating that a great deal of N and O atoms had been etched after increasing both the amount of KOH and activation temperature. CNPCNS-800 contained C (92.1 at%), O (5.4 at%) and N (2.6 at%). The content of N and O in the carbon nanosheets was attributed to the relative high content of N (26.2 at%) and O (23.9 at%) in adenosine. The C 1s, N 1s and O 1s spectra of NPCNS, CNPCNS-700, CNPCNS-800 and CNPCNS-900 were fitted by XPS peak software to further investigate their chemical states. Fig. 4b represents the high-resolution N 1s spectra of NPCNS, CNPCNS-700, CNPCNS-800 and CNPCNS-900. All curves exhibited three deconvoluted peaks attributed to pyridinic-N (N-6, 398.3 eV), pyrrolic-N (N-5, 400.2 eV) and quaternary N (N-Q, 402.6 eV).[33,34] N-6 and N-5 could generate pseudocapacitance for improving the capacitive performance, while N-Q could improve the conductivity of the carbon materials for increasing the rate performance. Fig. 4c represents the high-resolution O 1s spectra of NPCNS, CNPCNS-700, CNPCNS-800 and CNPCNS-900. Three types of oxygen species, including C=O (531.0 eV), C–O–C (532.3 eV) and O–C=O (533.3 eV), are presented on NPCNS,

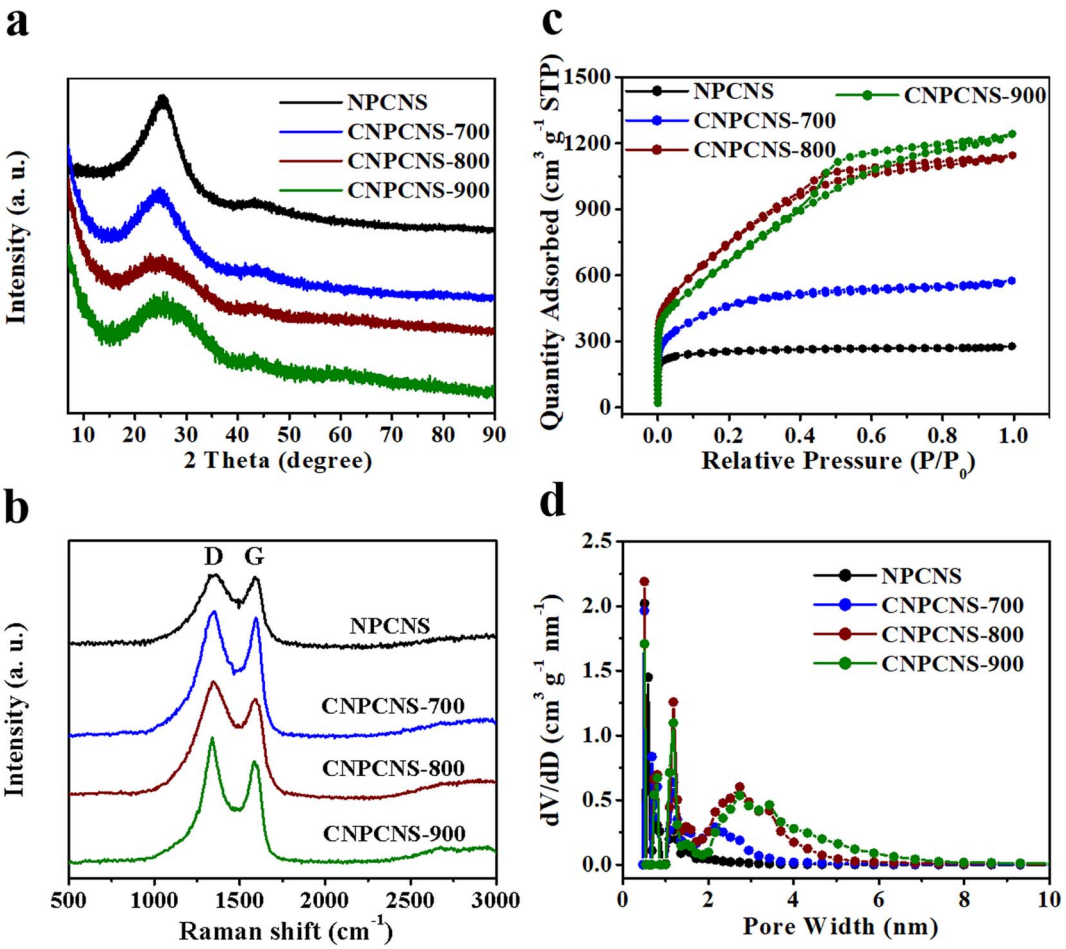

Fig. 3 (a) XRD patterns, (b) Raman spectra, (c) N_2 sorption isotherms and (d) density functional theory pore-size distributions of NPCNS, CNPCNS-700, CNPCNS-800 and CNPCNS-900.

Table 1 Pore structural parameters and XPS results of NPCNS, CNPCNS-700, CNPCNS-800 and CNPCNS-900

Sample	S_{BET} ($m^2\ g^{-1}$)	S_{micro} ($m^2\ g^{-1}$)	S_{micro}/S_{BET} (%)	V_{total} ($cm^3\ g^{-1}$)	V_{micro} ($cm^3\ g^{-1}$)	V_{micro}/V_{total} (%)	C (at%)	N (at%)	O (at%)
NPCNS	763	702	92.0	0.42	0.37	88.1	77.9	8.2	13.9
CNPCNS-700	1563	1252	80.1	0.88	0.61	69.3	80.7	6.7	12.6
CNPCNS-800	2756	1023	37.1	1.76	0.49	27.8	92.1	2.6	5.4
CNPCNS-900	2494	221	8.9	1.90	0.08	4.2	92.8	2.4	4.8

CNPCNS-700, CNPCNS-800 and CNPCNS-900.[34] The high-resolution C 1s spectra of CNPCNS-800 (Fig. 4d) and NPCNS, CNPCNS-700 and CNPCNS-900 (Fig. S7†) had four kinds of deconvoluted peaks that correspond to C–C (284.7 eV), –C–O/–C–N (285.8 eV), –C═O/–C═N (287.8 eV) and O–C═O (289.8 eV). These nitrogen and oxygen-containing species played important roles in improving the wettability of the porous carbon nanosheets.[35,36]

The electrochemical properties of NPCNS, CNPCNS-700, CNPCNS-800 and CNPCNS-900 were firstly evaluated in a three-electrode system in 6 M KOH. Fig. 5a displays the cyclic voltammetry (CV) curves of NPCNS, CNPCNS-700, CNPCNS-800 and CNPCNS-900 at 5 mV s^{-1}. NPCNS, CNPCNS-700, CNPCNS-800 and CNPCNS-900 exhibited a good quasi-rectangular shape with broad redox peaks, indicating the combination of the electric double-layer capacity (EDLC) storage mechanism and pseudocapacitive energy storage behavior.[37,38] Fig. S8† shows the CV curves of CNPCNS-800 at various scan rates. Even at 100 mV s^{-1}, the rectangular shape of the CV curve is still well retained, indicating a good capacitive behavior and excellent rate performance. Fig. 5b displays the galvanostatic charge discharge (GCD) curves of NPCNS, CNPCNS-700, CNPCNS-800 and CNPCNS-900 at 0.5 A g^{-1}. NPCNS, CNPCNS-700, CNPCNS-800 and CNPCNS-900 showed an ideal triangular shape with a small distortion, revealing excellent electrochemical reversibility. CNPCNS-800 clearly possessed a larger CV area and longer GCD charge/discharge time than NPCNS, CNPCNS-700 and CNPCNS-900, meaning that CNPCNS-800 had the largest

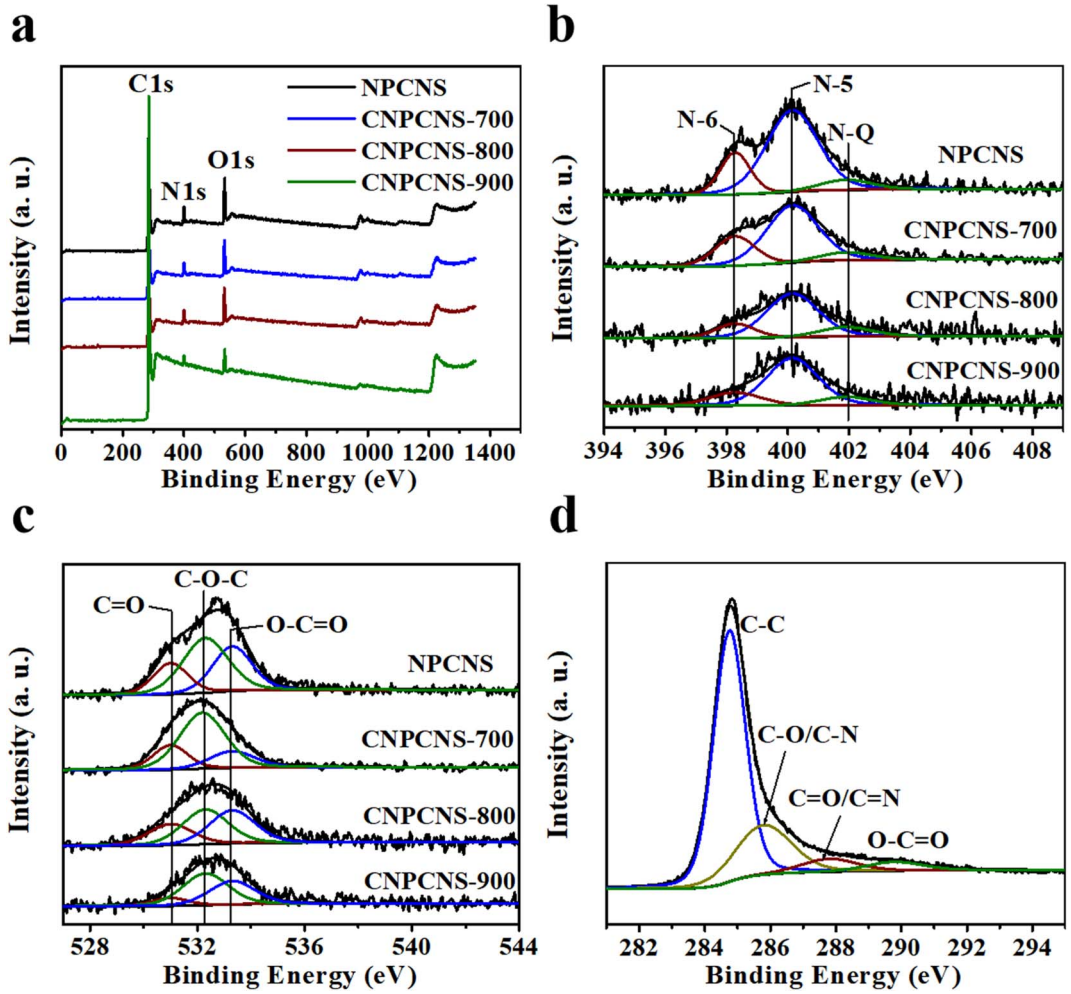

Fig. 4 (a) XPS survey, (b) N 1s and (c) O 1s spectra of NPCNS, CNPCNS-700, CNPCNS-800 and CNPCNS-900. (d) C 1s spectrum of CNPCNS-800.

specific capacitance. The specific capacitance curves of NPCNS, CNPCNS-700, CNPCNS-800 and CNPCNS-900 are shown in Fig. 5c. CNPCNS-800 had the highest specific capacitance among all samples. The specific capacitance of CNPCNS-800 was as high as 404 F g^{-1} at 0.5 A g^{-1}, which was superior to that of most of the current reported carbon nanosheets listed in Table 2. After an 80-fold increase of the current density, the capacitance of CNPCNS-800 could reach up to 240 F g^{-1}, which was much larger than those of NPCNS, CNPCNS-700 and CNPCNS-900. Moreover, the capacitance retention increases in the order of CNPCNS-900 (75%) > CNPCNS-800 (59%) > CNPCNS-700 (58%) > NPCNS (16%). Benefiting from their shorter ion diffusion pathways and much higher SSA, the crumpled porous carbon nanosheets showed much higher capacitance and rate performance than the flat porous carbon nanosheets. Compared with the flat porous carbon nanosheets, the crumpled porous carbon nanosheets had more advantages as follows: (1) the crumpled surface structure could effectively prevent the carbon nanosheets from stacking together in favor of increasing the high accessible SSA; (2) the ultrathin nanosheet with predominantly mesoporous structures was conducive to providing more electrolyte ion diffusion paths and short electrolyte ion transport lengths; (3) the ultrahigh SSA of the crumpled porous carbon nanosheets could adsorb a great deal of electrolyte ions. Benefiting from its extremely high mesopore proportion (S_{meso}/S_{BET} = 91.1%, V_{meso}/V_{total} = 95.8%), CNPCNS-900 showed the highest capacitance retention among the CNPCNS samples.

The superior electrochemical performance of CNPCNS-800 was further understood by the electrochemical impedance spectroscopy measurement. Fig. 5d displays the Nyquist plots of NPCNS, CNPCNS-700, CNPCNS-800 and CNPCNS-900, in which the nearly vertical line at the low frequency region revealed the EDLC behavior. In the high frequency region, the semicircle diameters of CNPCNS-800 and CNPCNS-900 were obviously smaller than those of NPCNS and CNPCNS-700, revealing their lower charge-transfer resistance and faster ion diffusion towards the surface. Although the microporous surface area and the content of N and O in CNPCNS-800 were lower than those of CNPCNS-700, the specific capacitance of CNPCNS-800 were superior to that of CNPCNS-700, which could be attributed to the highly mesoporous structure in CNPCNS-800 greatly

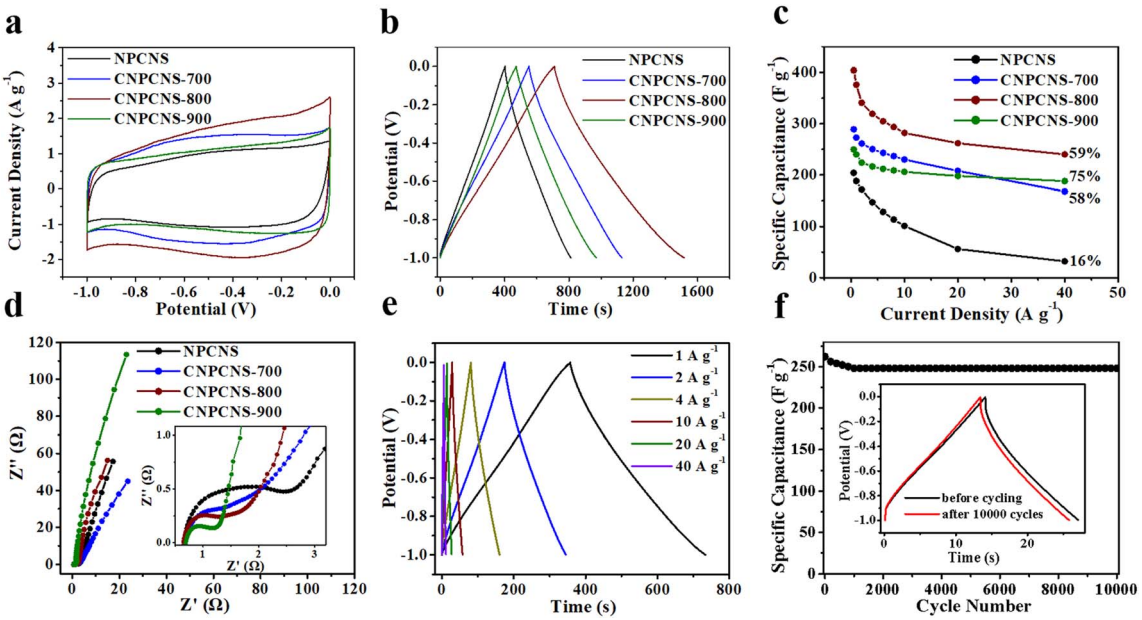

Fig. 5 (a) CV curves (5 mV s^{-1}), (b) GCD curves (0.5 A g^{-1}), (c) specific capacitances and (d) Nyquist plots of NPCNS, CNPCNS-700, CNPCNS-800 and CNPCNS-900 measured in 6 M KOH. (e) GCD curves and (f) cycling stability of CNPCNS-800 in 6 M KOH.

increasing the accessible microporous surface area and providing more diffusion channels for electrolyte ion adsorption and storage on the micropores. CNPCNS-900 had an ultrahigh mesoporous surface area, but exhibited very low specific capacitances compared to CNPCNS-800. This is because the very low microporous structure in CNPCNS-900 resulted in insufficient adsorption sites for electrolyte ion adsorption. In addition, as shown in Fig. 5e, the triangular shape of the GCD curves with low voltage drop was still well retained at 1, 2, 4, 10, 20 and 40 A g^{-1}, further demonstrating that CNPCNS-800 had excellent electrochemical reversibility and outstanding rate capability. After testing for 10 000 GCD cycles at 20 A g^{-1} (Fig. 5f), the capacitance retention of CNPCNS-800 was as high as 94.6%, indicating that CNPCNS-800 had outstanding cycling stability. The superior capacitance and rate capability of CNPCNS-800 were attributed to the crumpled nanosheet structure, the highest SSA with a high content of small-sized mesopores, as well as the appropriate incorporation of heteroatoms.

Table 2 Comparison of the specific capacitances of current reported carbon nanosheets in 6 M KOH

Materials	BET SSA (m^2 g^{-1})	Current density (A g^{-1})/scan rate	Specific capacitance (F g^{-1})	Ref.
Pillared-porous carbon nanosheet	883	2 mV s^{-1}	289	20
Porous carbon sheets anchored with ZIF-derived carbon	1352	0.2	326	25
Strutted porous carbon nanosheets	539	0.5	286	27
Crumpled nitrogen-doped graphene-like nanosheets	1169	0.5	294	30
Graphene-like porous carbon nanosheets	1051	1	294	31
Porous carbon nanosheets	1009	0.5	311	33
Ultrathin porous carbon nanosheets	962	1	306	35
Interlaced porous carbon nanosheets	731	0.5	247	39
Two-dimensional porous carbon nanosheets	1259.1	2 mV s^{-1}	232	40
B/N co-doped porous carbon nanosheets	880	0.2	360	41
Porous carbon nanosheets	1533	0.5	298	42
Highly porous carbon nanosheets	2266.6	0.1	384	43
Bark-based porous carbon nanosheet	2156	0.5	345	44
N/O co-doped porous carbon nanosheets	655	0.5	270	45
Sandwich-like porous carbon nanosheets	410.4	2 mV s^{-1}	305	46
Porous carbon nanosheets	986	1	280	47
B/N co-doped carbon nanosheets	817	1	257	48
Ultrathin carbon nanosheets	1535	0.5	347	49
CNPCNS	2756	0.5	404	This work

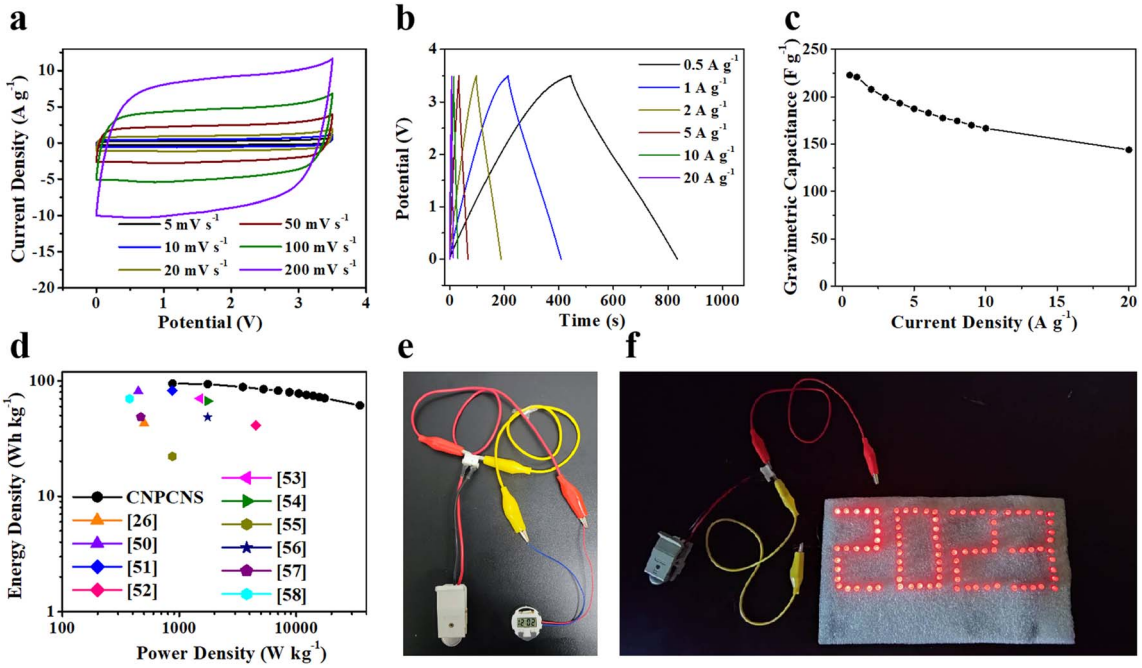

Fig. 6 (a) CV curves, (b) GCD curves and (c) specific capacitances of CNPCNS-800 based symmetrical supercapacitor in $EMIMBF_4$. (d) Comparison of the energy density of CNPCNS-800 with recently reported carbon materials in $EMIMBF_4$. Photographs of (e) one electronic watch and (f) 89 red light-emitting diodes bulbs by two CNPCNS-800 based symmetric supercapacitors in series.

The 1-ethyl-3-methylimidazolium tetrafluoroborate ($EMIMBF_4$) electrolyte with high operating voltage window and high electrochemical and thermal stability has been intensively used as electrolyte in carbon-based supercapacitors for improving energy density. To further evaluate and verify the superb electrochemical performance of CNPCNS-800, a symmetric supercapacitor was assembled by two identical CNPCNS-800 electrodes in $EMIMBF_4$. Fig. 6a displays the CV curves of the CNPCNS-800-based supercapacitor. All CV curves exhibited an ideal quasi-rectangular shape with a high operating voltage up to 3.5 V, indicating a good capacitive behavior and excellent rate performance. The linear and symmetrical triangular shape of the GCD curves in Fig. 6b indicate a predominant EDLC behavior. The specific capacitances derived from the GCD curves are shown in Fig. 6c. The specific capacitance of CNPCNS-800 at 1 A g^{-1} could reach up to 221 F g^{-1}, which was higher than that previously reported for advanced carbon nanomaterials in $EMIMBF_4$ at 1 A g^{-1}, such as interconnected carbon nanosheets (122 F g^{-1}),[22] hierarchical porous carbon nanosheets (173 F g^{-1}),[50] interconnected carbon nanocages (194 F g^{-1}),[51] and carbon nanoparticles (129 F g^{-1}).[52] Despite the high viscosity and low ionic conductivity of $EMIMBF_4$, a very high capacitance retention of 64.5% was retained even at 20 A g^{-1} (144 F g^{-1}), revealing the good rate capability of CNPCNS-800. The high specific capacitance and rate capability of CNPCNS-800 in $EMIMBF_4$ electrolyte could be attributed to the crumpled nanosheets structure and abundant mesoporous structures facilitating faster ion transport and fully utilizing the high SSA (2756 m^2 g^{-1}). Fig. S9† shows the 5000 GCD cycling test of CNPCNS-800 at 10 A g^{-1}. The very high capacitance retention of 93.2% directly illustrates its outstanding cycling stability. Fig. 6d shows the Ragone plot of CNPCNS-800. Due to the high capacitance and wide working potential range, the energy density of CNPCNS-800 could reach up to 94.9 W h kg^{-1} at a power density of 875 W kg^{-1}, which was superior to that of the recently reported carbon-based supercapacitors in $EMIMBF_4$.[26,50–58] The energy density of CNPCNS-800 still remained as high as 61.2 W h kg^{-1} even at 35 kW kg^{-1}. Therefore, one electronic watch (Fig. 6e) and 89 red LED bulbs aligned in "2023" shape (Fig. 6f) could be easily lighted by two CNPCNS-800-based supercapacitors connected in series, demonstrating their potential application in supercapacitors.

Conclusions

In conclusion, we provide a novel strategy to prepare the crumpled nitrogen-doped porous carbon nanosheets (CNPCNS) with an ultrahigh SSA and a hierarchical pore structure, as well as ultrathin crumpled nanosheets doped with nitrogen. In this strategy, adenosine acted as both carbon/nitrogen source and expansive agent to form nitrogen-doped carbon nanosheets. Meanwhile, KOH was used as an activator to form the crumpled nanosheet morphology. The crumpled morphology allowed CNPCNS to hinder its tendency to stack together, leading to CNPCNS having a much greater accessible specific surface area and faster electrolyte ion diffusion channel. Therefore, CNPCNS exhibited a high specific capacitance, rate capability, and long cycle life both in 6 M KOH and ionic liquid electrolyte. Most importantly, the symmetric supercapacitor assembled by two identical CNPCNS in ionic liquid displayed an ultrahigh energy

density. This work not only provided a new avenue for producing CNPCNS for high-performance supercapacitors, but also opened new doors to design new materials with CNPCNS for electrocatalysts, water purification, rechargeable Li^+/Na^+ batteries and other applications.

Author contributions

C. Chen, J. C. Shao and L. Sun designed the experiments. J. C. Shao and Y. R. Zhang carried out the electrochemical performance tests. K. Y. Zhang and H. Y. Wang provided characterizations *via* SEM, TEM, XRD, XPS, Raman and N_2 absorption–desorption tests. C. Chen and G. Zhu wrote the paper.

Conflicts of interest

The authors declare no competing financial interests.

Acknowledgements

This work is financially supported by the National Natural Science Foundation of China (22002103), the Natural Science Foundation of Anhui Provincial (2008085QB77, 2108085MB67), The Key project of Natural Science Research of Anhui Education Department (KJ2021A1103, KJ2021ZD0138, KJ2016A888, KJ2020A0730), Quality Engineering Project of Anhui (2020rcsfjd42, 2021xsxxkc297), Bio-based Functional Materials and Composite Technology Research Center (2021XJPT06), Open Research Projects of Suzhou University (2022ykf23), Foundation of Suzhou University (2022xhx135, 2022xhx136, 2022xhx145), Scientific Research and Development Fund Project of Suzhou University (2021fzjj16), Primary Research and Development Program of Anhui Province (201904a05020087), and Professor (doctor) of the Suzhou University Scientific Research Foundation Project (2019jb02, 2021BSK012).

References

1 S. H. Shi, Y. L. Tang, G. Z. Wang, W. Z. Yu, G. P. Wan, L. H. Wu, Z. Deng and G. L. Wang, *Nano Energy*, 2022, **96**, 107132.
2 G. Q. Zhao, G. P. Wan, Y. L. Tang, X. F. Xu, X. C. Zhou, M. F. Zhou, Z. Deng, S. W. Lin and G. Z. Wang, *Chem. Commun.*, 2020, **56**, 12435–12438.
3 S. H. Shi, G. P. Wan, L. H. Wu, Z. Y. He, K. Wang, Y. L. Tang, X. F. Xu and G. Z. Wang, *J. Colloid Interface Sci.*, 2019, **537**, 142–150.
4 S. Saini, P. Chand and A. Joshi, *J. Energy Storage*, 2021, **39**, 102646.
5 C. Chen, Y. Z. Xu, J. C. Shao, Y. R. Zhang, M. T. Yu, L. Sun, H. Y. Wang, Y. Xie, G. Zhu, L. Zhang and L. K. Pan, *J. Colloid Interface Sci.*, 2022, **616**, 413–421.
6 Y. Zhang, L. Zhang, L. Cheng, D. D. Yang, L. Wan, C. Du, J. Chen and M. J. Xie, *Appl. Surf. Sci.*, 2021, **538**, 148040.
7 L. Jiang, S. H. Yang, W. N. Song, J. H. Zhao, Z. H. Lu, Q. Q. Zhai and J. Wang, *ChemNanoMat*, 2020, **6**, 308–315.
8 Y. F. Bu, T. Sun, Y. J. Cai, L. Y. Du, O. Zhuo, L. J. Yang, Q. Wu, X. Z. Wang and Z. Hu, *Adv. Mater.*, 2017, **29**, 1700470.
9 F. B. Su, C. K. Poh, J. S. Chen, G. W. Xu, D. Wang, Q. Li, J. Y. lin and X. W. Lou, *Energy Environ. Sci.*, 2011, **4**, 717–724.
10 X. X. Zhu, X. H. Huang, S. Anwer, N. Y. Wang and L. D. Zhang, *Langmuir*, 2020, **36**, 9284–9290.
11 S. W. Bokhari, A. H. Siddique, P. C. Sherrell, X. Y. Yue, K. M. Karumbaiah, S. H. Wei, A. V. Ellis and W. Gao, *Energy Rep.*, 2020, **6**, 2768–2784.
12 Y. L. Shao, M. F. El-kady, L. J. Wang, Q. H. Zhang, Y. G. Li, H. Z. Wang, M. F. Mousaviae and R. B. Kaner, *Chem. Soc. Rev.*, 2015, **44**, 3639–3665.
13 X. B. Wang, Y. J. Zhang, C. Y. Zhi, X. Wang, D. M. Tang, Y. B. Xu, Q. H. Weng, X. F. Jiang, M. Mitome, D. Golberg and Y. Bando, *Nat. Commun.*, 2013, **4**, 2905.
14 Y. W. Zhu, S. Murali, M. D. Stoller, K. J. Ganesh, W. W. Cai, P. J. Ferreira, A. Pirkle, R. M. Wallace, K. A. Cychosz, M. Thommes, D. Su, E. A. Stach and R. S. Ruoff, *Science*, 2011, **332**, 1537–1541.
15 H. L. Fan and W. Z. Shen, *ChemSusChem*, 2015, **8**, 2004–2027.
16 Y. F. He, X. D. Zhuang, C. J. Lei, L. C. Lei, Y. Hou, Y. Y. Mai and X. L. Feng, *Nano Today*, 2019, **24**, 103–119.
17 K. Jayaramulu, D. P. Dubal, B. Nagar, V. Ranc, O. Tomanec, M. Petr, K. K. R. Datta, R. Zboril, P. Gómez-Romero and R. A. Fischer, *Adv. Mater.*, 2018, **30**, 1705789.
18 Y. S. Yun, S. Y. Cho, J. Y. Shim, B. H. Kim, S. J. Chang, S. J. Baek, Y. S. Huh, Y. Tak, Y. W. Park, S. Park and H. J. Jin, *Adv. Mater.*, 2013, **25**, 1993–1998.
19 L. Yao, J. S. Lin, H. T. Yang, Q. Wu, D. R. Wang, X. J. Li, L. B. Deng and Z. J. Zheng, *Nanoscale*, 2019, **11**, 11086–11092.
20 Z. J. Fan, Y. Liu, J. Yan, G. Q. Ning, Q. Wang, T. Wei, L. J. Zhi and F. Wei, *Adv. Energy Mater.*, 2012, **2**, 419–424.
21 D. W. Wang, F. Li, M. Liu, G. Q. Lu and H. M. Cheng, *Angew. Chem., Int. Ed.*, 2008, **47**, 373–376.
22 H. L. Wang, Z. W. Xu, A. Kohandehghan, Z. Li, K. Cui, X. H. Tan, T. J. Stephenson, C. K. King'ondu, C. M. B. Holt, B. C. Olsen, J. K. Tak, D. Harfield, A. O. Anyia and D. Mitlin, *ACS Nano*, 2013, **6**, 5131–5141.
23 M. Sevilla and A. B. Fuertes, *ACS Nano*, 2014, **5**, 5069–5078.
24 A. B. Fuertes and M. Sevilla, *ACS Appl. Mater. Interfaces*, 2015, **7**, 4344–4353.
25 Z. M. Shen, Y. H. Mo, J. Du and A. B. Chen, *Appl. Surf. Sci.*, 2020, **527**, 146845.
26 C. Chen, D. F. Yu, G. Y. Zhao, B. S. Du, W. Tang, L. Sun, Y. Sun, F. Besenbacher and M. Yu, *Nano Energy*, 2016, **27**, 377–389.
27 C. Chen, M. K. Zhao, Y. Y. Cai, G. Z. Zhao, Y. Xie, L. Zhang, G. Zhu and L. K. Pan, *Carbon*, 2021, **179**, 458–468.
28 W. M. A. E. Rouby, *RSC Adv.*, 2015, **5**, 66767–66796.
29 J. Y. Luo, H. D. Jang and J. X. Huang, *ACS Nano*, 2013, **2**, 1464–1471.
30 H. Peng, G. Ma, K. Sun, Z. Zhang, Q. Yang, F. Ran and Z. Q. Lei, *J. Mater. Chem. A*, 2015, **3**, 13210–13214.
31 B. Liu, M. Yang, H. B. Chen, Y. J. Liu, D. G. Yang and H. M. Li, *J. Power Sources*, 2018, **397**, 1–10.

32 E. Raymundo-Piñero, P. Azaïs, T. Cacciaguerra, D. Cazorla-Amorós, A. Linares-Solano and F. Béguin, *Carbon*, 2005, **43**, 786–795.

33 M. Wang, J. Yang, S. Liu, M. Li, C. Hu and J. S. Qiu, *J. Colloid Interface Sci.*, 2020, **560**, 69–76.

34 J. L. Figueiredo and M. F. R. Pereira, *Catal. Today*, 2010, **150**, 2–7.

35 M. Y. Liu, J. Niu, Z. P. Zhang, M. L. Dou and F. Wang, *Nano Energy*, 2018, **51**, 366–372.

36 X. Y. Chen, C. Chen, Z. J. Zhang and D. H. Xie, *J. Mater. Chem. A*, 2013, **1**, 10903.

37 Y. J. Oh, J. J. Yoo, Y. I. Kim, J. K. Yoon, H. N. Yoon, J. Kim and S. B. Park, *Electrochim. Acta*, 2014, **116**, 118–128.

38 W. J. Zhang, Z. T. Chen, X. L. Guo, K. Jin, Y. X. Wang, L. Li, Y. Zhang, Z. M. Wang, L. T. Sun and T. Zhang, *Electrochim. Acta*, 2018, **278**, 51–60.

39 J. W. Yang, Z. X. Tan, X. Chen, Y. R. Liang, M. T. Zheng, H. Hu, H. W. Dong, X. R. Liu, Y. L. Liu and Y. Xiao, *J. Colloid Interface Sci.*, 2021, **599**, 381–389.

40 S. Y. Bai, C. X. Fan, L. L. Li and X. L. Wu, *Electroanal. Chem.*, 2021, **886**, 115119.

41 Y. H. Yao, G. G. Huang, Y. B. Liu, Y. Liu, Y. Y. Li, G. X. Han, B. L. Xing, Q. R. Liu, J. B. Jia and C. X. Zhang, *Appl. Surf. Sci.*, 2022, **580**, 152236.

42 Y. J. Li, G. L. Wang, T. Wei, Z. J. Fan and P. Yan, *Nano Energy*, 2016, **19**, 165–175.

43 Y. Z. Wang, Y. Liu, W. Liu, G. X. Zhang, G. W. Liu, H. Y. Chen and J. L. Yang, *J. Alloys Compd.*, 2016, **677**, 105–111.

44 Y. Li, S. M. Liu, Y. Liang, Y. Xiao, H. W. Dong, M. T. Zheng, H. Hu and Y. L. Liu, *ACS Sustainable Chem. Eng.*, 2019, **7**, 13827–13835.

45 B. Liu, Y. J. Liu, H. B. Chen, M. Yang and H. M. Li, *J. Power Sources*, 2017, **341**, 309–317.

46 Q. Wang, J. Yan and Z. J. Fan, *Electrochim. Acta*, 2014, **146**, 548–555.

47 L. Miao, D. Z. Zhu, M. X. Liu, H. Duan, Z. W. Wang, Y. K. Lv, W. Xiong, Q. J. Zhu, L. C. Li, X. L. Chai and L. H. Gan, *Chem. Eng. J.*, 2018, **347**, 233–242.

48 J. Li, Y. Dong, J. Y. Zhu, L. X. Wang, W. H. Tian, J. Zhao, H. Lin, S. Zhang, Y. L. Cao, H. H. Song and D. Z. Jia, *Appl. Surf. Sci.*, 2020, **529**, 147239.

49 K. M. Zhao, S. Q. Liu, G. Y. Ye, Q. M. Gan, Z. Zhou and Z. He, *J. Mater. Chem. A*, 2018, **6**, 2166–2175.

50 D. F. Yu, C. Chen, G. Y. Zhao, L. Sun, B. S. Du, H. Zhang, Z. Li, Y. Sun, F. Besenbacher and M. Yu, *ChemSusChem*, 2018, **11**, 1–9.

51 D. W. Wang, Y. T. Wang, H. W. Liu, W. Xu and L. Xu, *Chem. Eng. J.*, 2018, **342**, 474–483.

52 D. D. Chen, Z. Q. He, M. Wang, D. Wu, X. Y. Chen and Z. J. Zhang, *J. Solid State Electrochem.*, 2020, **24**, 641–654.

53 C. Chen, H. Y. Wang, Q. G. Xiao, M. K. Zhao, Y. J. Li, G. Z. Zhao, Y. Xie, X. Y. Chen and G. Zhu, *Ind. Eng. Chem. Res.*, 2019, **58**, 22124–22132.

54 F. Y. Liu, Z. X. Wang, H. T. Zhang, L. Jin, X. Chu, B. N. Gu, H. C. Huang and W. Q. Yang, *Carbon*, 2019, **149**, 105–116.

55 Y. B. Zhou, J. Ren, L. Xia, Q. J. Zheng, J. Liao, E. Y. Long, F. Y. Xie, C. G. Xu and D. M. Lin, *Electrochim. Acta*, 2018, **284**, 336–345.

56 H. F. Pan, Y. M. Zhang, Y. F. Pan, W. R. Lin, W. M. Tu and H. N. Zhang, *Chem. Eng. J.*, 2020, **401**, 126083.

57 Y. L. Wang, B. B. Yang, D. Y. Zhang, H. Shi, M. Lei, H. X. Li and K. J. Wang, *Appl. Surf. Sci.*, 2020, **512**, 145711.

58 X. D. Liu, M. M. Vadiyar, J. K. Oh and Z. B. Ye, *ACS Appl. Mater. Interfaces*, 2021, **13**, 32916–32929.